

Data Analysis

Aerosol Studies

Measuring Dust Absorption from MODIS and Landsat

Airborne dust from Africa or the Gobi Desert in Asia intercepts incoming sunlight, reflecting a portion back to space and absorbing another fraction of the solar radiation. Reflection acts to cool the atmosphere by decreasing the amount of radiation retained by the system. Absorption acts to heat the atmosphere by keeping the radiation within the system. The balance between reflection and absorption determines if dust can heat or cool the climate.

There may be a feedback between dust emission and climate change, since large amounts of dust are emitted from the deserts in dry years, like the maximum El Niño year of 1987. Therefore, depending on the ability of dust to absorb sunlight, it can produce a positive or negative feedback on the climate system. What we mean is that in a hot year, when drier deserts emit large amounts of absorbing dust into the atmosphere, the additional dust will result in additional heating of the atmosphere and may result in even more dust being emitted. However, if dust is not very absorbing the situation may be reversed. Of course, this is a very simplistic way to look on the effect of dust since atmospheric circulation is not as simple as depicted, and detailed global climate models are needed to really assess the dust effect. The simple model described above only illustrates the profound importance of knowing exactly how much desert dust really absorbs.

Until recently, the scientific community believed Saharan dust to be a strong absorber of sunlight, because it includes rust (iron oxide) that gives the red color to soils in Africa. Bermuda also boasts red soils, which were brought to the islands from Africa by the easterly winds. Figure 6-9 (right panel) shows the dust caught up in the easterly wind that transports the dust across the Atlantic to the islands and continents of the Western Hemisphere. Working with visiting scientists from France and Israel on a totally unrelated problem, we found that dust models published in 1983 by the World Meteorological Organization cannot explain analysis of Landsat data from a 1987 French experiment in Western Africa. Using newer reports of dust models gave the same inconsistent results. Thus we decided to use the MODIS data to generate a new model of dust absorption. Using the data from the images in Figure 6-9, our analysis is demonstrated in Figure 6-10.



Figure 6-9. MODIS images of Western Africa and the Atlantic Ocean. (a) left image without dust, Jan. 27, 2001 (b) right image showing dust emitted from Africa over the Atlantic Ocean and moving toward the Americas, Feb. 12, 2001. These images illustrate the type of data set necessary for the dust absorption analysis shown in Figure 6-10. The clear day reflectance, the abscissa, is taken from Figure 6-9 left, while the dust reflectance, the ordinate, is obtained from the difference of Figures 6-9 right and left.

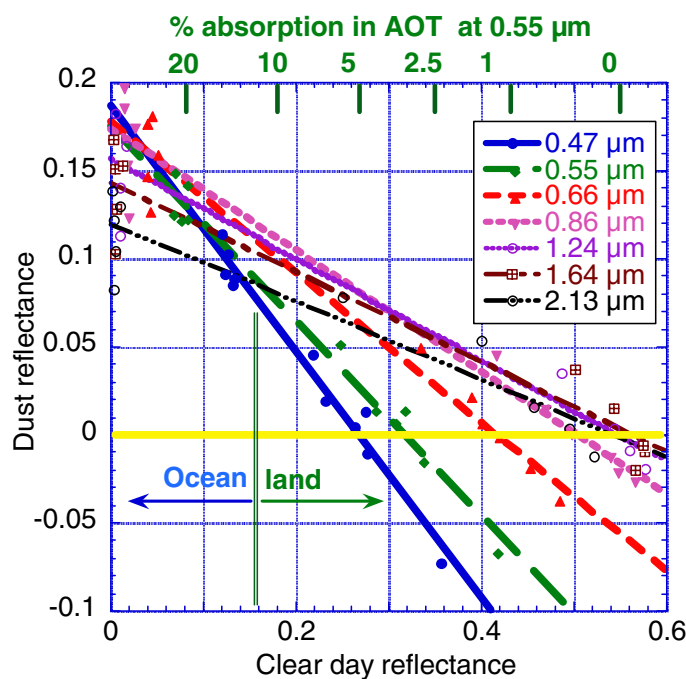


Figure 6-10. Dust reflectance of sunlight, meaning the difference in the reflectance measured by MODIS in a day with dust and a day with no dust, plotted as a function of the land reflectance in the day with no dust. The dust reflectance can be positive or negative, depending on the dust absorption and land reflectance. The brighter the land, the stronger the influence of dust absorption and the more negative the dust reflectance is. From the value of surface reflectance for which the dust reflectance is zero, we deduce the fraction of the dust optical thickness corresponding to absorption. The corresponding values of absorption percentage for the 0.55 μm channel are given at the top of the figure. The figure is plotted for all the relevant solar channels of MODIS from 0.47 μm to 2.1 μm .

Using the MODIS and Landsat data, we found that dust is not absorbing in the red to near IR channels (the green line in Figure 6-11). It is absorbing in the blue and UV parts of the spectrum, but much less than the absorption used in models currently accepted by the community. Once these new optical properties are included in numerical climate models, the significantly lower dust absorption and correspondingly higher dust reflection of sunlight will show that dust has a cooling effect. Meanwhile, in situ measurement techniques of dust absorption have improved. Preliminary measurements of dust outbreaks from Asia and Africa were presented recently in the IAMAS meeting in Austria and indicate similarly low dust absorption from the new in situ measurements.

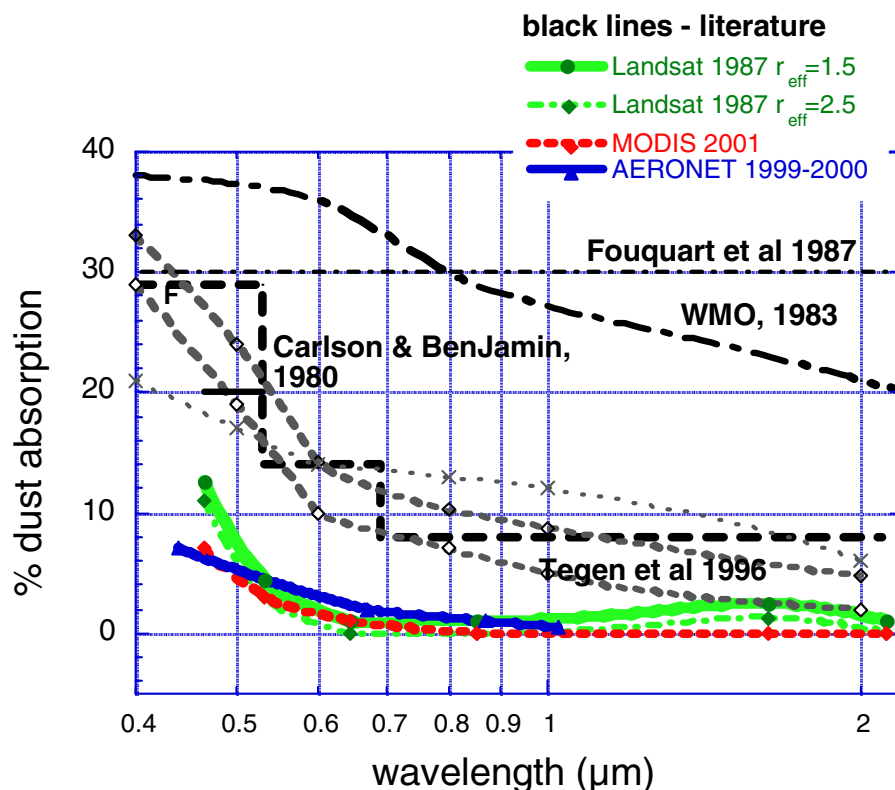


Figure 6-11. The spectral absorption of dust given as the % of the dust optical thickness. The green lines are the analysis of Landsat data for 1987 for two assumed sizes of the dust particles, the red line is the analysis of the MODIS data for 2001, and the blue line is the analysis of ground-based measurements by the Aerosol Robotic Network instruments in Capo Verde, an Island in the Atlantic Ocean off the African coast. All of them show very similar results. The black lines are different models from the World Meteorological Organization model (WMO) and from different papers published in the last few years.

Yoram Kaufman and Lorraine Remer, Code 913 (Yoram.Kaufman.1@gsfc.nasa.gov)

Climatic and Ecological Impacts of Asian Dusts

Recently intensified Asian dust storms have called attention to the topic of aerosol radiative forcing of climate, a phenomenon that constitutes a major source of uncertainty in climate change research. These dust storms occur frequently in arid and semi-arid areas of northwestern China in the springtime. To better understand the properties of dust aerosols, we deployed the SMART (Surface Measurements for Atmospheric Radiative Transfer) remote-sensing system during the ACE-Asia (March-May 2001) study.

Our work took place in the vicinity of Dun-Huang, China. Dun-Huang is located at one of the largest oases between the Taklimakan and the Gobi Deserts. It is in the source region of dust storms without much manmade contamination. Figures 6-12 & 6-13 demonstrate the sky conditions before, during, and after the impact of a dust storm.



Figure 6-12. Dust storm is approaching the Dun-Huang site (left panel) and the researchers have scrambled for shelter; photo taken at 3 p.m. local time on 28 April 28 2001. The fierce storm has generated a dense blanket of dust in the air, just 1 hour after the event (right panel).

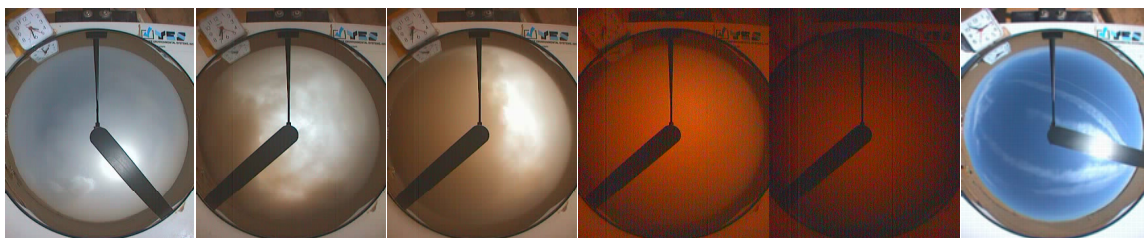


Figure 6-13. Time series of images captured by the Whole Sky Camera depict a dust storm passing through the Dun-Huang site. The last image reveals that many contrails streak across a clear blue sky.

Dust storms have the potential for enormous social impact. Nearly half the world's population resides in Asia, and China alone is home to roughly 1.3 billion people. These masses rely on crops produced from 8% of the world's farmland and on the yield from fisheries of the surrounding oceans. Airborne dust particles might alter regional hydrological cycles by direct and indirect radiative forcing. Dust storms might affect fisheries by influencing the nutrient deposition pattern. The storms might also produce adverse health effects on humans (e.g., irritating the eyes and respiratory system with aluminum, zinc, and iron contained in the dust aerosols). In addition, these dust clouds can transport swiftly across the Pacific reaching North America within a few days (*cf.* NASA press release in April 2001).

The seasonal incidence of dust storms peaks from March to May. The number of storms has tripled in recent years, from a 30-year average of 3.5 events per year to 10 events in 2000. ACE–Asia focused primarily on dust radiative forcing on regional to global climate. The optical depths (at 0.5 μm wavelength) of dusts during ACE–Asia (near the source region of Dun-Huang oasis, China) averaged about 0.8, with a maximum of greater than 2. The dust layers were almost always present at the surface. In Figure 6-14, all cloud-free data, based on Sun photometer and whole-sky camera observations, are used to quantify the radiative forcing of dust aerosols. Since atmospheric energetics requires integration over a period of time, the air mass (solar zenith angle) should be introduced as a parameter. The slopes ($\Delta F/\Delta\tau$, as shown in the right panel of Figure 6-14) of each slice of air mass depict the solar radiative forcing at the surface; their values clustered around -134 W m^{-2} (cooling) at local solar noon.

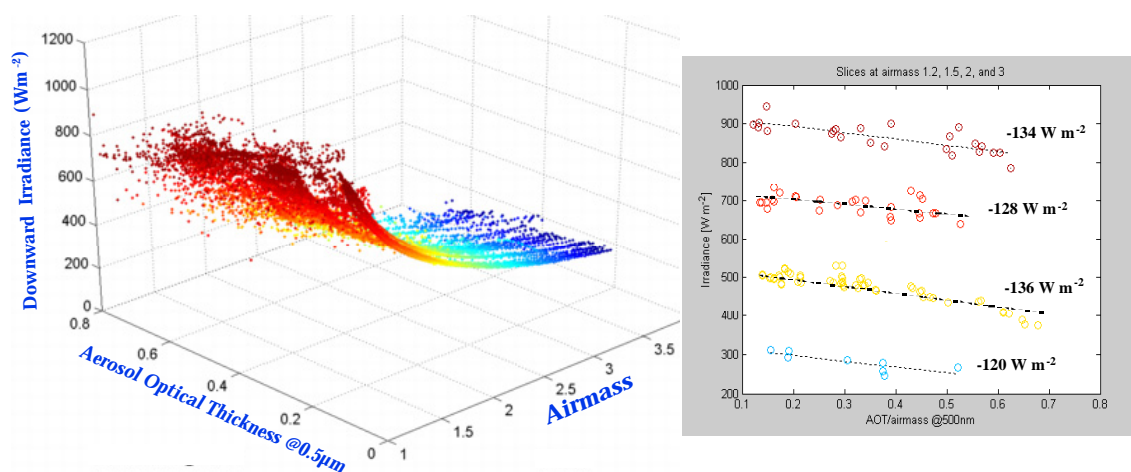


Figure 6-14. Three-dimensional representation of surface radiative forcing by dust aerosols during ACE–Asia from March to May 2001.

Si-Chee Tsay, Code 913 (Si-Chee.Tsay.1@gsfc.nasa.gov)

Modeling of Tropospheric Aerosols

Aerosol radiative forcing is one of the largest uncertainties in assessing global climate change. We have recently developed an atmospheric aerosol model to help us understand the various processes that control aerosol properties and to understand the roles of aerosols in atmospheric chemistry and climate. The model is called the Georgia Tech/Goddard Global Ozone Chemistry Aerosols Radiation and Transport (GOCART) model.

GOCART uses the meteorological fields produced by the Goddard Data Assimilation Office (DAO), code 910.3, and includes major types of aerosols: sulfate, dust, black carbon, organic carbon, and sea salt. Among these, sulfate, black and organic carbon mainly originate from human activities, such as fossil fuel combustion and biomass burning. Dust and sea salt are mainly generated by natural processes; for example, uplift of dust from a desert by strong winds.

We have compared extensively the model results with satellite, aircraft, and surface observations. Our comparisons enable us to evaluate the model and, more importantly, to interpret the data. Figure 6-15 shows the comparison of total aerosol optical thickness calculated from the GOCART model with that retrieved from the satellite measurement by Total Ozone Mapping Spectrometer (TOMS). Here, the model reproduces the most prominent features as seen in the satellite data. Examples are biomass burning over equatorial northern Africa in January, a large dust plume originating in North Africa and transporting across the Atlantic Ocean in July, and biomass burning aerosols over southern Africa in July and over Brazil in October. The high optical thickness over Indonesia in October, revealed by both model and TOMS, is due to the unusually intensive biomass burning that occurred during fall 1997. Over the tropical or subtropical ocean, however, the aerosol optical thickness from the model is much lower than that from the TOMS. This difference occurs partly because of the difficulties involved in the TOMS retrieval when aerosols are optically thin. It is also possible that the model underestimates the aerosol source from the tropical ocean.

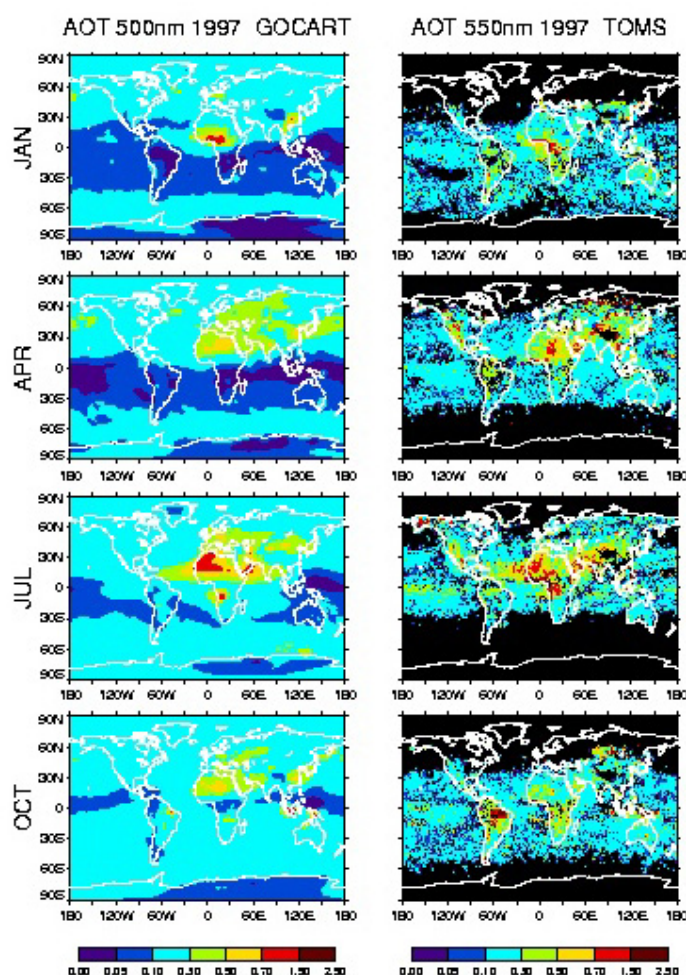


Figure 6-15. Aerosol optical thickness in 1997 from the GOCART model (left column) and the TOMS retrieval (right column). TOMS data are from Torres et al., 2001.

Figure 6-16 shows the comparison of model-calculated aerosol optical thickness with the quantities directly measured by the Sun photometer in the Aerosol Robotic Network (AERONET). Also shown in Figure 6-16 is the model-estimated aerosol composition. At Mongu (southern Africa), carbonaceous aerosol is the dominating aerosol from the biomass burning, which has a very strong seasonal variation and peaks in September. By contrast, almost all aerosols from Cape Verde (west coast off northern Africa) are dust from the Sahara region. At the NASA GSFC location, sulfate aerosol level is usually higher than other aerosol types, while the aerosol composition at Bermuda varies with the season.

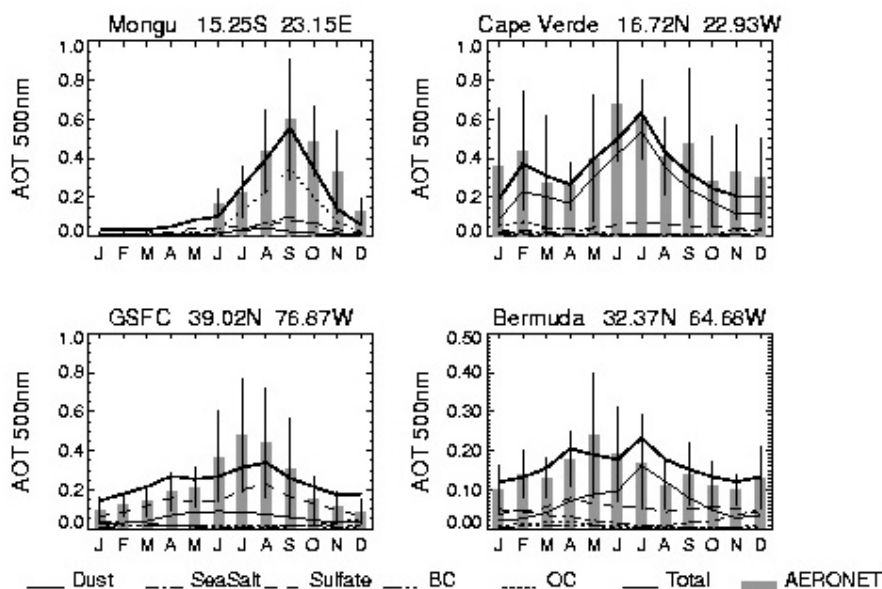


Figure 6-16. Comparison of aerosol optical thickness calculated in the model with that measured at four AERONET sites. Data are from Holben et al., 2001.

The detailed description of this work appears in the Special Issue of Global Aerosol Climatology of the Journal of the Atmospheric Sciences: Chin, M. and 9 others, 2001: Tropospheric aerosol optical thickness from the GOCART model and comparisons with satellite and sun photometer measurements.

The model assessment of aerosol's impact on future climate has been included in the 2001 Intergovernmental Panel on Climate Change (IPCC) report. Using the projected future emission change due to the change of human activities and emission controls, we have estimated the aerosol optical thickness and direct radiative forcing in the present and in 2030 and 2100. We have found that, on a global average, the direct aerosol forcing at the top of the atmosphere is almost linearly related to the emission of aerosols and their precursors.

In spring 2001, the intensive field phase for the ACE–Asia took place over the Asian-Pacific region. ACE–Asia is a multinational, multiagency-sponsored field program with a goal of improving our understanding of how aerosols, transported from the Asian continent, influence the chemical and radiative properties of the Earth's atmosphere. We have been actively involved in the ACE–Asia program. During the intensive field operation period (March–May 2001), we provided aerosol forecasts using the meteorological forecasts (including winds, temperature, clouds) from the DAO. Figure 6-17 gives an example of the GOCART model forecast of aerosol optical thickness for dust, sulfate (mainly from pollution), and black carbon (mainly from biomass burning), as well as the cloud forecast from DAO for April 8, 2001. These products were used every day at the field operation center for planning optimal flight routes.

We are currently working on model analysis of the ACE–Asia data to evaluate the controlling processes that determine the aerosol properties and distributions of Asian aerosols and their effects on the Earth's climate.

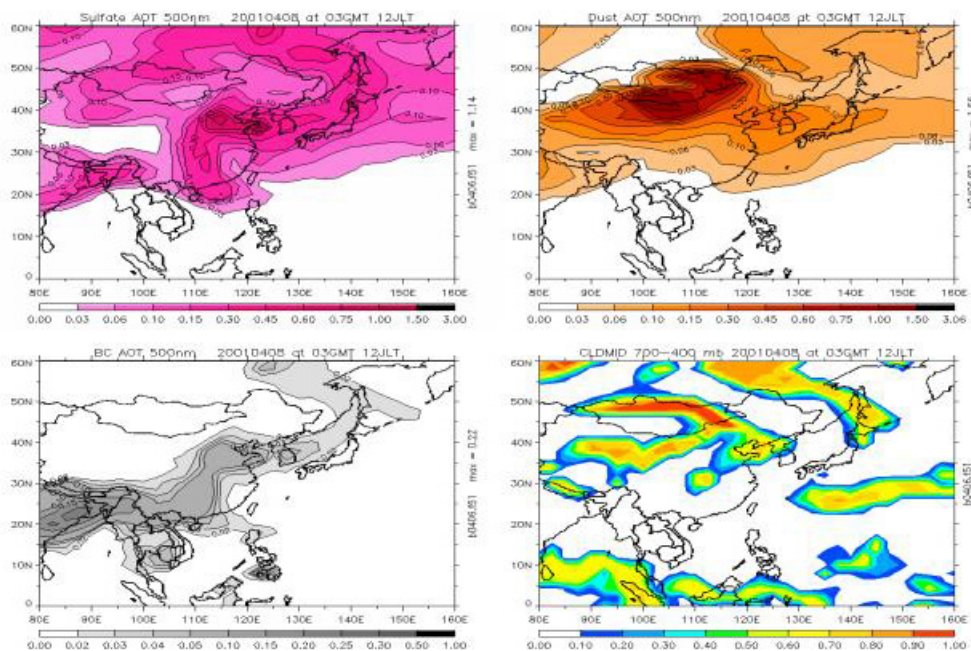


Figure 6-17. Model forecast of aerosol optical thickness of sulfate, dust, and black carbon at 500nm for April 8, 2001. Also shown is the midlevel cloud fraction forecasted by the DAO.

Mian Chin, Code 916 (Mian.Chin.1@gsfc.nasa.gov)

Studies of Radiative Forcing of Saharan Dust Aerosols

We used satellite data to determine the direct radiative forcing over Saharan dust. In our analysis, we combined aerosol information from Nimbus-7 TOMS with top of the atmosphere radiation (TOA) measurements from NOAA-9 ERBE. We used cloud and precipitable water information from NOAA-9 HIRS to screen for clouds and water vapor.

Our results indicate that under *cloud-free* and *dry* conditions a good correlation exists between the ERBE TOA outgoing longwave fluxes and the TOMS aerosol index measurements over both land and ocean in areas under the influence of airborne Saharan dust. We also found the ERBE TOA outgoing shortwave fluxes to correlate well with the dust loading derived from TOMS over ocean. However, the calculated shortwave forcing of Saharan dust aerosols is very weak and noisy over land for the range of solar zenith angle viewed by the NOAA-9 ERBE in 1985. Forcing efficiency of the TOA outgoing fluxes due to Saharan dust was estimated using a linear regression fit to the ERBE and TOMS measurements.

Figure 6-18 summarizes our results. The ratio of the shortwave-to-longwave response to changes in dust loading over the ocean is found to be roughly 2 to 3, but opposite in sign. It indicates a net cooling effect in the atmosphere over ocean. The effect can locally be as much as 15 Watts/m² in February and 25 Watts/m² in July. However, due to the weak response of the shortwave radiation to the change in dust loading over arid land, the net radiation budget is dominated by the longwave wavelength response, resulting a net warming.

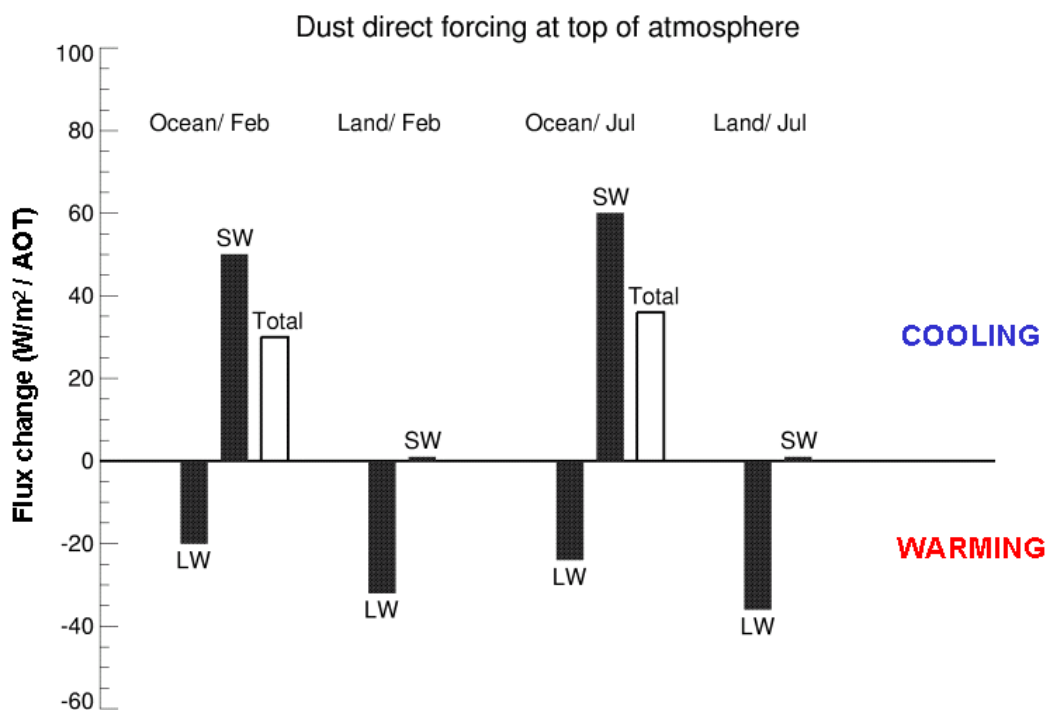


Figure 6-18. Summary of the estimated TOA longwave and shortwave direct forcing of dust per unit AOT over land and ocean surfaces for February and July.

Both the observational and theoretical analyses indicate that the underlying surface properties, the dust-layer height, the ambient moisture content, and the presence of clouds all play important roles in determining the TOA direct radiative forcing due to mineral aerosols.

During the past year, these techniques have been applied to the recent large Asian dust storm (The Perfect Dust Storm) originating in the Gobi and Taklamaken Deserts and reaching across the Pacific Ocean and into the U.S. (Figure 6-19). Another key result is that the amount of dust appearing over China has increased annually since the start of the TOMS data (1979) and most strongly in recent years according to data from Earth-Probe/TOMS. The radiative forcing for the ACE-Asia Perfect Dust Storm was comparable to that from the Saharan Dust, about 15 Watts/m².

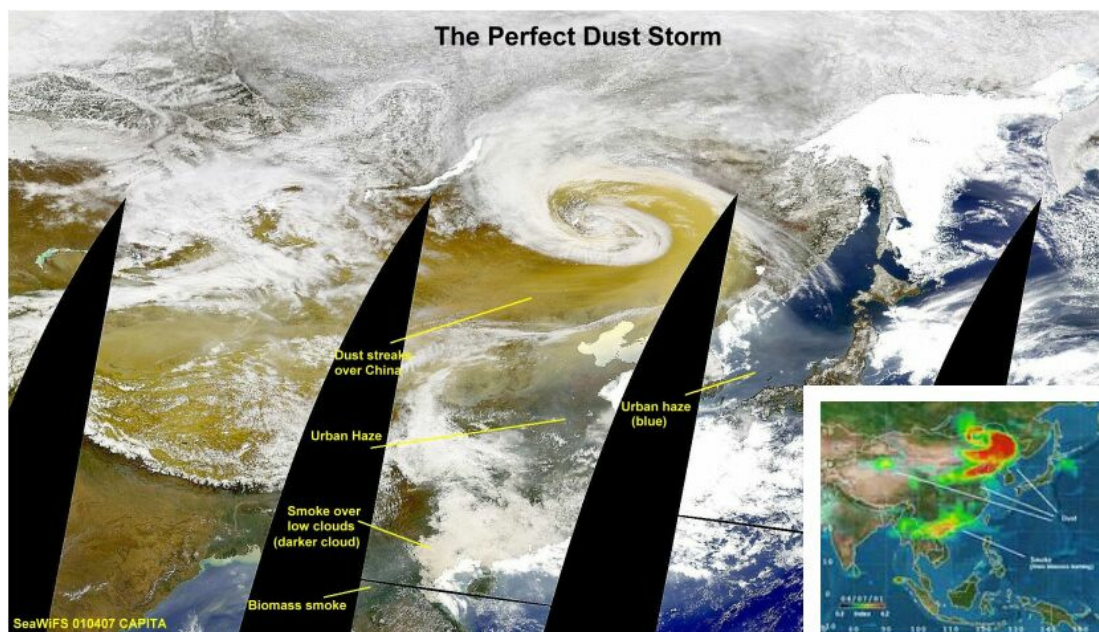


Figure 6-19. “The Perfect Dust Storm” from SeaWiFS observations and the aerosol observations from TOMS.

Hsu, N. Christina, Herman, J.R., and Clark Weaver, Determination of Radiative Forcing of Saharan Dust Using Combined TOMS and ERBE Data, *J. Geophys. Res.*, **105**, 20649-20662, 2000.

Jay R. Herman and Christina Hsu, Code 916 (Jay.R.Herman.1@gsfc.nasa.gov)

Atmospheric Chemistry

Extremely Cold Temperatures and the Absence of Polar Stratospheric Clouds during SOLVE

The Airborne Raman Ozone Temperature and Aerosol Lidar (AROTEL) made observations that were both unexpected and significant during the recently concluded Sage III Ozone Loss and Validation Experiment (SOLVE) mission. AROTEL is a collaborative effort between Goddard Space Flight Center and Langley Research Center.

SOLVE took place during the winter of 1999/2000. The mission focused on processes controlling stratospheric ozone levels from the northern mid-latitudes to the North Pole. Polar stratospheric clouds, or PSCs, are a major component in the loss of polar ozone. PSCs provide the surfaces on which chemically inactive reservoir species convert to active species capable of destroying ozone.

Temperature plays a key role in the formation and lifetime of PSCs. In part because of temperature's pivotal role, AROTEL was selected to fly on NASA's DC-8 to provide high-resolution profiles of the arctic temperature fields. Lidar retrievals from the DC-8 offer distinct advantages over satellite data. They provide high-precision temperature profiles along with measurements of ozone, aerosols, clouds, and water vapor throughout the region of interest. These measurements were designed to help understand the conditions under which PSCs form and persist by identifying regions in the lower Arctic stratosphere where temperatures were low enough for PSCs to persist (195 K or lower).

AROTEL measured extremely cold temperatures during all three SOLVE deployments (December, 1999; January, 2000; and February–March, 2000). Temperatures were significantly below values observed in previous years, with large regions regularly below 191 K and frequent retrievals gave temperatures at or below 187 K. Temperatures were regularly encountered well below the saturation point of Type I PSCs, but their presence was not well correlated with PSC observations made by AROTEL. On December 12, extensive regions were observed having temperatures as cold as 185 K. Simultaneous observations on AROTEL's aerosol and polar stratospheric cloud (PSC) channels captured few, if any, PSCs within these extremely cold regions.

These observations are both surprising and important. Current theories on PSCs predict the occurrence of PSCs for measured values of nitric acid and water vapor at these temperatures. PSC formation depends critically on an air parcel's temperature and time history, its altitude, and the mixing ratio profiles of nitric acid and water vapor. The absence of PSCs where conditions appear favorable for their existence suggests that our current understanding of PSC formation is incomplete. The series of figures below illustrate this important conclusion.

Figure 6-20 displays over 7 hours of temperature data from the December 12th flight. This flight originated in Kiruna, Sweden, flying north of Russia and Scandinavia to ~80N. Only temperatures between 185 and 195 K are presented and extensive regions at or below 189 K are clearly seen.

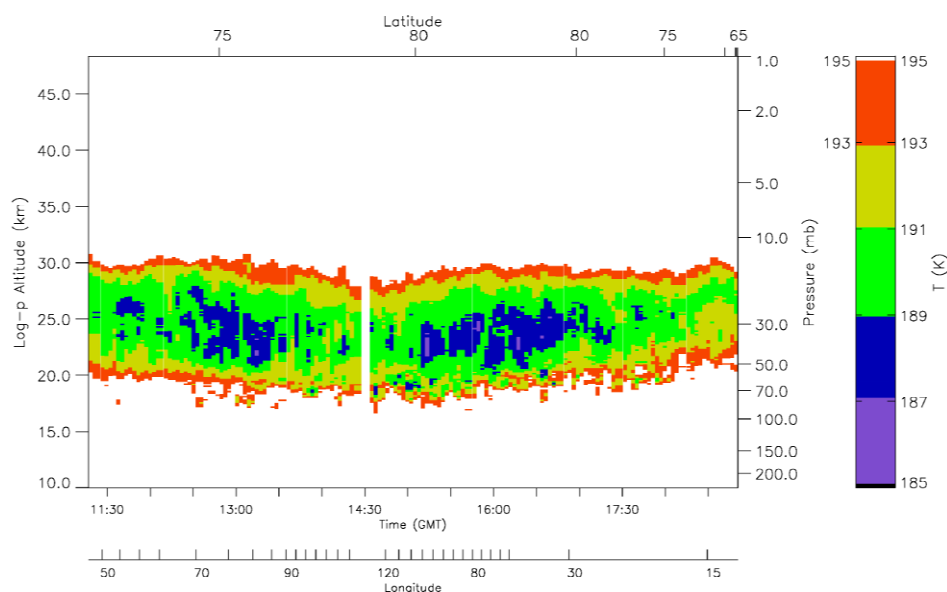


Figure 6-20. AROTEL temperatures between 185 and 195 K on flight of December 12, 1999.

Figure 6-21 shows the aerosol depolarization ratios measured on AROTEL's 532 nm channel. This data is used to identify PSCs that are nonspherical. Nonspherical PSCs are type 1a and type 2 PSCs, and Nat Rocks. Nat Rocks are very large particles >3 microns in diameter and having a very low number density. Nat rocks were first detected during SOLVE using in situ and AROTEL data. The figure shows that minimal depolarization was observed, meaning that nonspherical PSCs were absent.

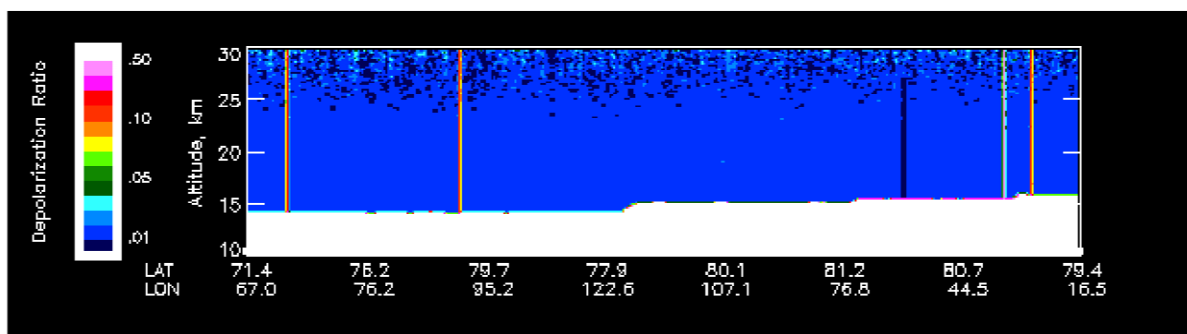


Figure 6-21. Aerosol depolarization on December 12th flight. The absence of depolarization indicates that nonspherical PSCs were absent between 15 to 30 km altitude on this flight.

Figure 6-22 presents aerosol backscattering as observed on AROTEL's 1064 nm channel. Mie scattering from PSCs and aerosols at this wavelength is typically much stronger than the weak molecular backscattering. Spherical PSCs (type 1b) are differentiated from background signals using this data and temperature. These observations are consistent with an aerosol background layer.

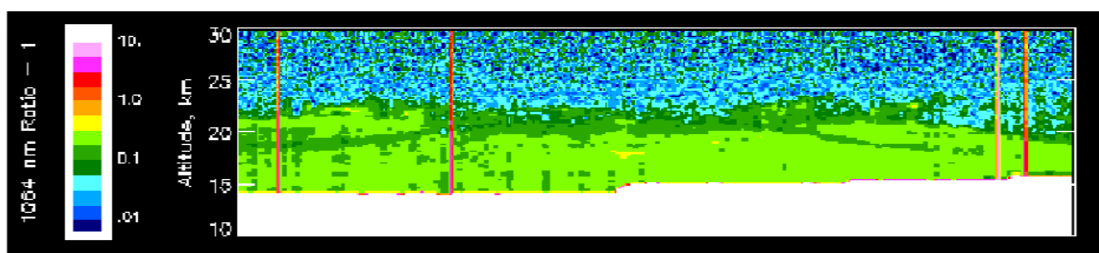


Figure 6-22. Aerosol backscattering at 1064 nm. Signal is consistent with only background aerosols being present.

Figure 6-23 displays four separate data sets addressing the December 12 observations. Aerosol/PSC backscattering as seen on the AROTEL 1064 nm channel appears in the upper left plot. AROTEL temperatures appear in the upper right plot. The bottom plots present calculations showing where Type 1 and 2 PSCs could exist as a function of temperature, nitric acid, and water vapor. (The lower left plot used AROTEL temperatures; the lower right plot used temperatures from Goddard's DAO). The dotted line in the bottom two plots separates data from regions where PSCs could exist (above line) from data that could not have originated from PSCs (below dotted line). In the lower left plot, only ~150 out of 168,000 acquired data points lie above the line. Below the line, the red dots represent temperatures where Type 1 PSCs should occur, but are not observed due to the low measured backscatter. Below the line, the yellow dots represent temperatures where Type 2 PSCs should occur, but also are not observed. The lower right panel uses DAO model temperatures, which are about 5 K higher than the measured AROTEL temperatures, and the red region below the dotted line indicates where PSCs should occur but are not observed.

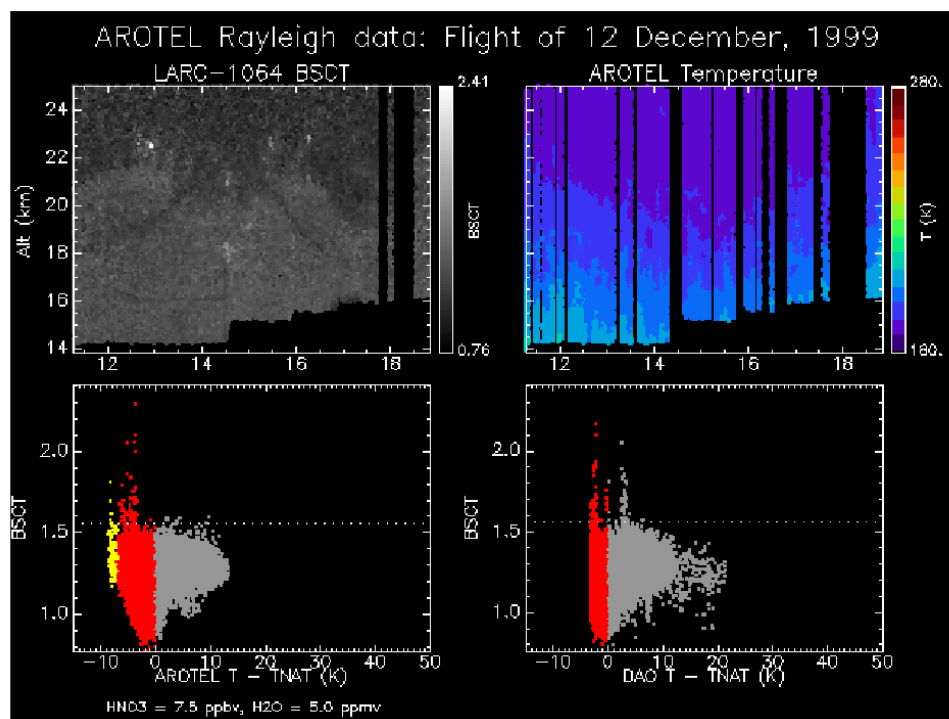


Figure 6-23. Upper left plot displays AROTEL 1064 nm backscatter data for December 12, 1999. Upper right plot shows AROTEL temperature data within the same region. Lower left plot shows where PSCs could exist as a function of measured AROTEL temperatures, water vapor, and nitric acid. Ordinate on the lower panels is the backscatter value and the abscissa is the difference between the AROTEL or DAO temperature and the Nat formation temperature. Data below the dotted line originated with aerosols and not PSCs; data above the dotted line originated with PSCs. The points above the dotted line consisted of only ~150 points out of a total of 168,000. The lower right plot is identical to the lower left one except that DAO temperatures were used in place of the measured values.

John F. Burris, Code 916 (John.F.Burris.1@gsfc.nasa.gov)

Measured Arctic Ozone Loss during the SOLVE Campaign

The SAGE III Ozone Loss and Validation Campaign (SOLVE) was conducted from Kiruna, Sweden, during the winter of 1999–2000. The campaign was an international effort and included the NASA DC-8 and the NASA ER-2 aircraft, both equipped to measure chemical and meteorological parameters. The Laboratory's Atmospheric Chemistry and Dynamics Branch (Code 916) flew the Airborne Raman Ozone Temperature and Aerosol Lidar (AROTEL) instrument on board the DC-8 for this mission. This instrument retrieves vertical profiles of ozone, temperature, aerosols, and clouds above the nominal flight altitude of 12 km.

One of the primary purposes of the mission was to document the concentration of stratospheric ozone as the Sun began to illuminate the Arctic vortex. The AROTEL instrument was an ideal instrument for this purpose, since it not only measures a vertical profile of ozone, but it also provides information as to the location and type of PSCs and the temperature environment as the PSCs form.

The campaign was made up of three deployments of the DC-8 to Kiruna. The first, in December 1999, sampled the prewinter Arctic atmosphere; a January deployment made measurements during the darkness of the winter; and the third deployment, in March 2000, observed large ozone losses and the breakup of the vortex. Figure 6-24 shows the ozone field above the aircraft during one of the flights in January, prior to any significant ozone loss. This flight took place almost entirely within the vortex and is indicative of the atmosphere within the vortex during January. For this reason all the data collected from within the vortex during all the January flights were averaged to obtain a “presunlight,” vortex ozone profile. Figure 6-25 shows similar data from the flight of March 13, 2000, and shows significant chemically related ozone loss particularly in the 18 km region. Data from within the vortex during the DC-8 flights on March 11 and March 13 were averaged and then compared with the January baseline profile to retrieve an ozone loss rate profile, which is shown in Figure 6-26. This plot indicates that the maximum ozone loss rate occurred at about 460K (approximately 18 km). The maximum loss rate obtained in this manner is 0.029 ppm/day. Shortly after the March 13 flight, the vortex began to break up and the ozone-depleted air began mixing with mid-latitude stratospheric air parcels.

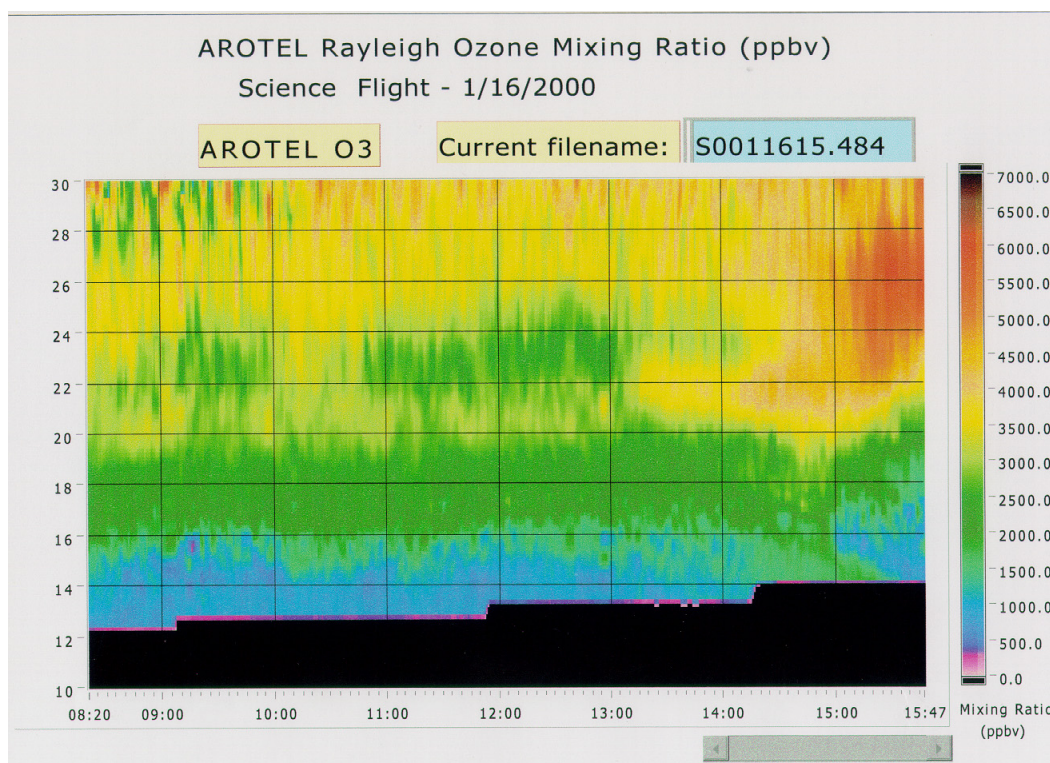


Figure 6-24. The vertical distribution of ozone above the NASA DC-8 during the flight of January 16, 2000.

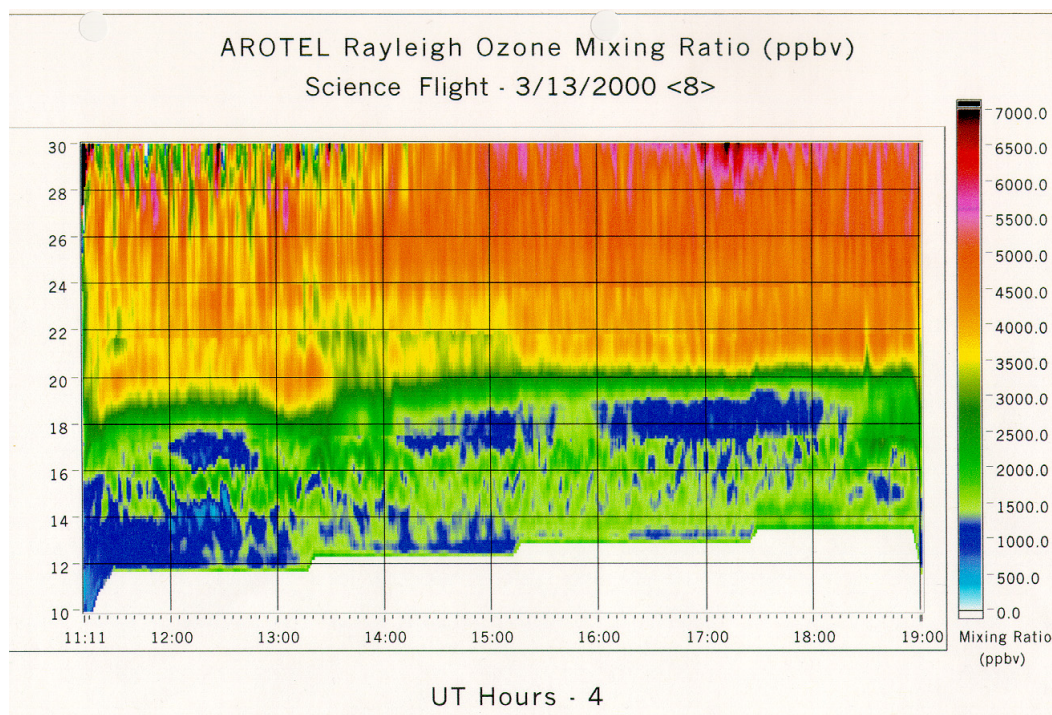


Figure 6-25. The vertical distribution of ozone above the NASA DC-8 for the flight of March 13, 2000.

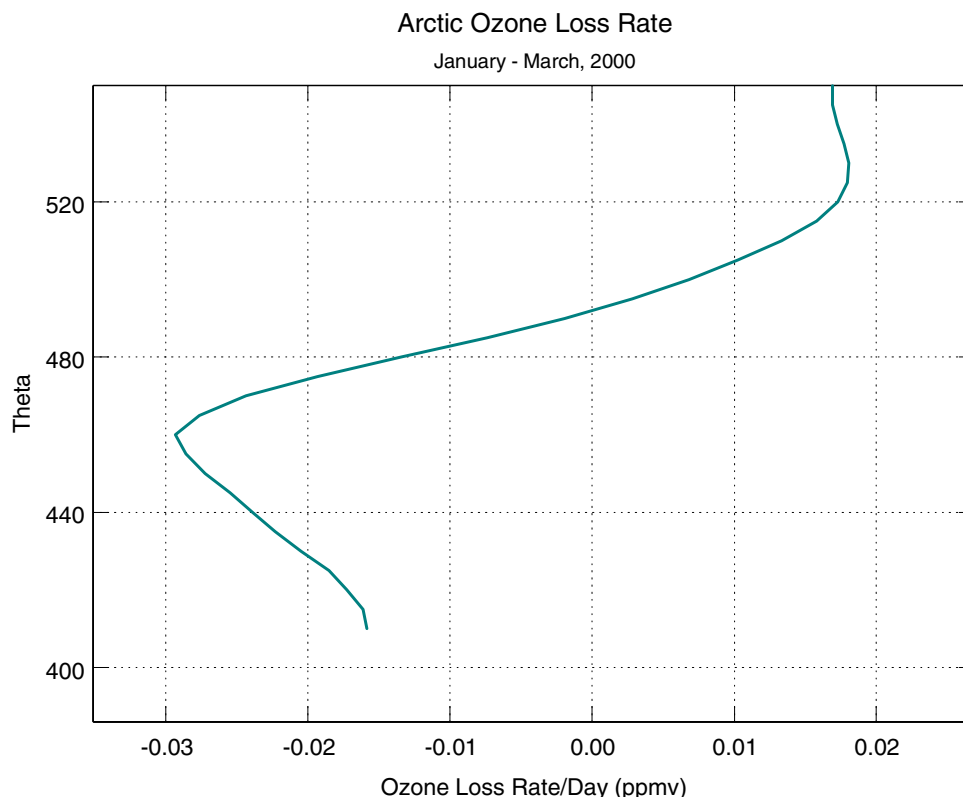


Figure 6-26. Plot showing the ozone loss rate from the January average vortex profile to the average of the vortex ozone during the flights of March 11 and 13, 2000.

Thomas J. McGee and John F. Burris, Code 916 (Thomas.J.McGee.1@gsfc.nasa.gov)

Changes in the Earth's UV Reflectivity from the Surface, Clouds, and Aerosols

Measurements of the Earth's 380 nm ultraviolet (UV) reflectivity combine the effects of surface reflectivity, aerosols, haze, cloud optical thickness and the fraction of the scene covered by clouds. Changes in UV cloud and aerosol reflectivity imply similar changes over a wide range of wavelengths—UV, visible, and near infrared (at least 0.31 to 2 microns). These changes affect both the transmission of radiation to the Earth's surface and the reflection back to space. TOMS (Total Ozone Mapping Spectrometer) 380 nm reflectivity data indicates that the 14-year annual mean power reflected back to space is $385.3 \pm 31 \text{ w/m}^2$. Most of the reflection is by clouds, aerosols, and snow/ice. Based on measured long-term changes in global reflectivity, it is estimated that there is an additional $2.8 \pm 2.8 \text{ w/m}^2$ per decade reflected back to space (2 standard-deviation error estimate) during the TOMS observing period of 1979 to 1992. Since the 380 nm surface reflectivity is low (2% to 8%) over most surfaces, water and land, the observed reflectivity changes are mostly caused by changes in the amount of snow/ice, cloudiness, and aerosols.

Time-series analysis of TOMS reflectivity over the period from 1979 to 1992 shows that no significant changes occurred in annually averaged zonal-average reflectivity at latitudes within 60°S to 60°N, even though there were changes at higher latitudes (e.g., 3% per decade, in reflectivity units, between 60°N and 70°N). When the effects of the 11-year solar cycle and ENSO (El Niño Southern Oscillation) are removed from the data, we observe statistically significant reflectivity changes poleward of both 40°S and 40°N (Figure 6-27). The solar-cycle results suggest a possible Sun-weather relationship.

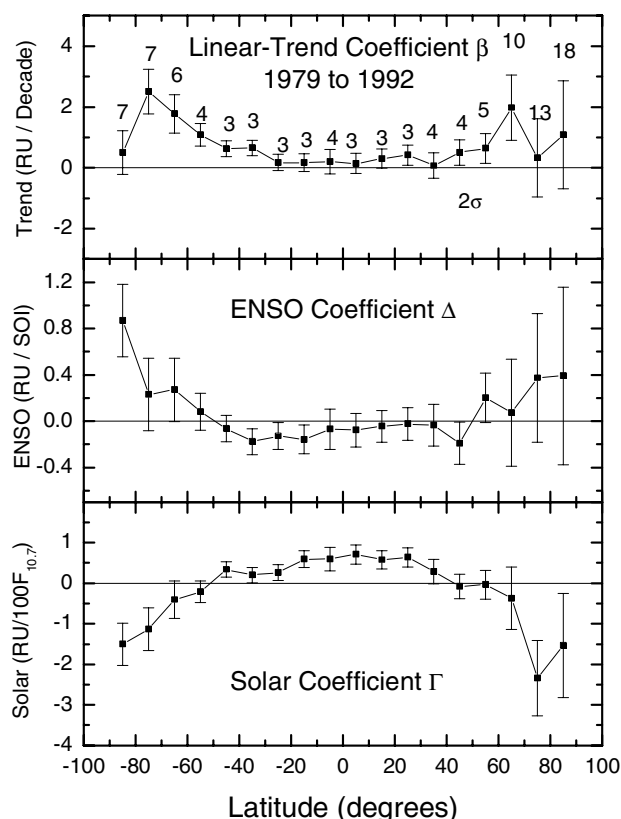


Figure 6-27. The linear-trend coefficient (upper panel) β ENSO coefficient Δ (middle panel), and the solar coefficient γ (lower panel) in units of RU per year, RU per SOI, and RU per 100 $F_{10.7}$, respectively. Error bars are 2σ standard deviations. 1 RU = 1% reflectivity.

There are significant regional changes over land and ocean areas that can affect the amount of solar radiation reaching the surface (Figure 6-28). The largest of these regions have decreases of 3 to $6 \pm 1\%$ per decade in central Europe, the western United States, central China, and western Russia. These decreases are offset by increases in the same latitude bands mostly over the oceans. The largest regions showing an increase in scene reflectivity are off the western coast of South America (near Chile and Peru), 5 to $8 \pm 1\%$ /decade, and over the Weddell Sea in Antarctica, 10% /decade. Yet no change appears over the ice shelf and continent. The largest increase in reflectivity occurs over the ocean just to the north of Antarctica. This change is important because it reduces UV radiation overall (290 to 400 nm), and it partially offsets the effect of the increased amount of UVB radiation (290 to 320 nm) caused by decreasing Antarctic ozone.

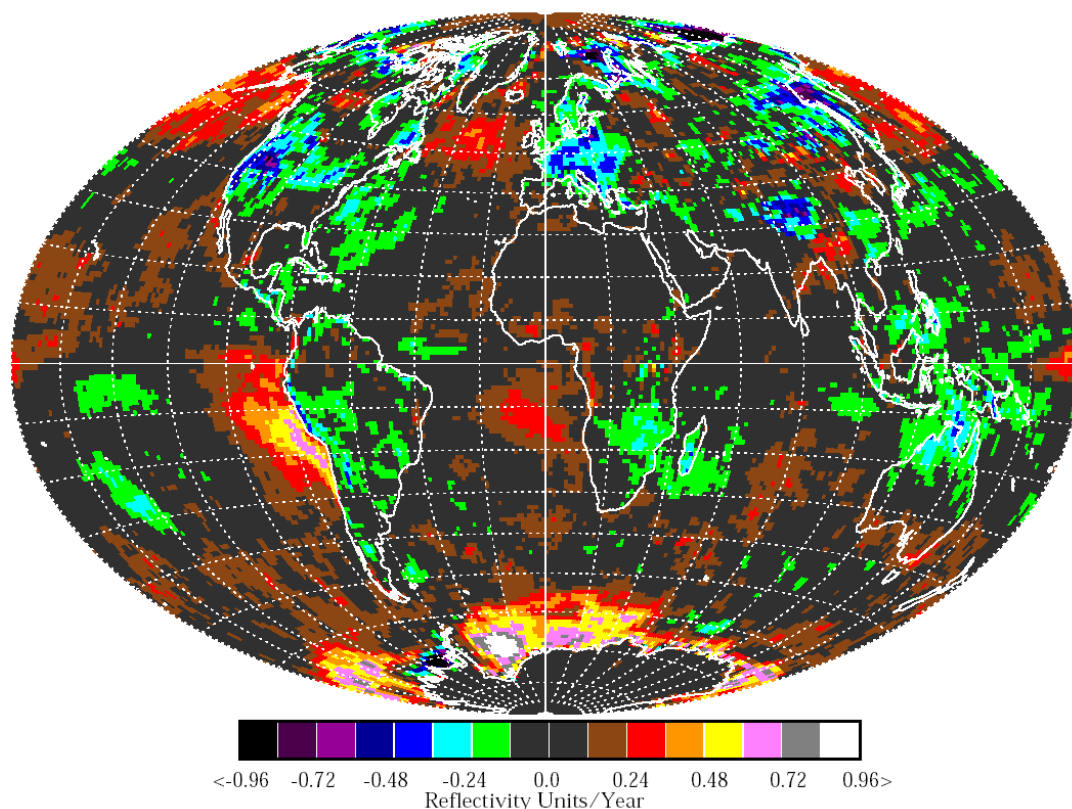


Figure 6-28. Contour plot of the linear slope coefficient (RU per year) for all causes (see Figure 6-27) showing a map of the global trends in annually averaged reflectivity for 1980 to 1992 for each $1^\circ \times 1^\circ$ TOMS pixel from the gridded reflectivity data set.

Herman, J.R., D. Larko, and J. Ziemke, Changes in the Earth's Global UV Reflectivity from Clouds and Aerosols, *J. Geophys. Res.* **106**, 5353-5368, 2001.

Jay R. Herman, Code 913 (Jay.R.Herman.1@gsfc.nasa.gov)

Global Mapping of Underwater UV Irradiances

The global stratospheric ozone-layer depletion results in an increase in biologically harmful UV radiation reaching the surface and penetrating to ecologically significant depths in natural waters. Such an increase can be estimated on a global scale by combining satellite estimates of UV irradiance at the ocean surface from the TOMS satellite instrument with the SeaWiFS satellite ocean-color measurements in the visible spectral region. We have developed a model of seawater optical properties in the UV spectral region based on the Case 1 (open ocean) water model in the visible range. The inputs to the model are standard monthly SeaWiFS products: chlorophyll concentration and the diffuse attenuation coefficient at 490nm. The depth of penetration of solar UV radiation (to 10% of surface intensity, Z10) into ocean water is shown in Figure 6-29

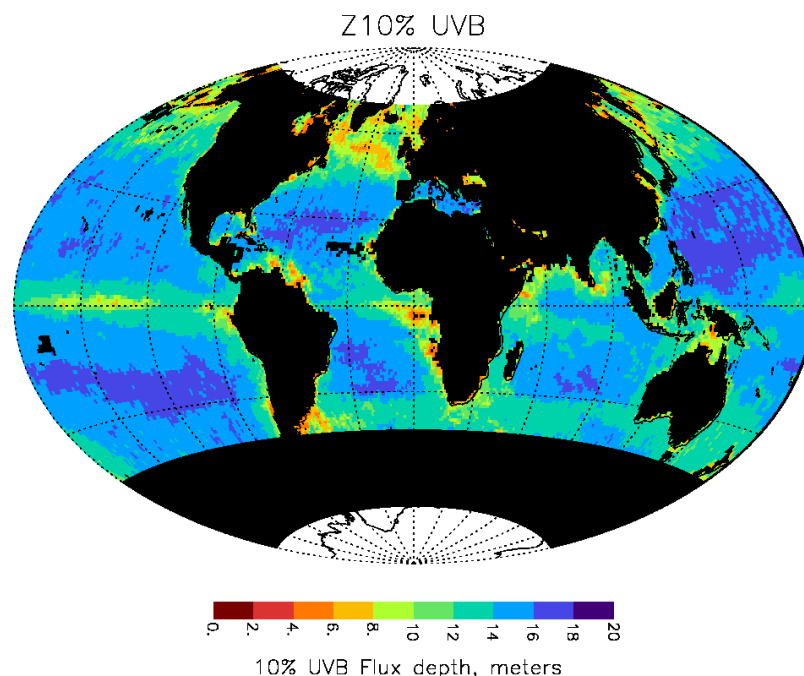


Figure 6-29. The depth of UVB penetration to level of 10% of the surface irradiance as a function of the input parameters: chlorophyll concentration and the diffuse attenuation coefficient at 490 nm.

Vasilkov, A., N. Krotkov, J. Herman, C. McClain, K. Arrigo, and W. Robinson, Global mapping of underwater uv fluxes and dna-weighted exposures using TOMS and SeaWiFS data products, *J. Geophys. Res.* Vol. 106, 27,205, 2001.

Sensitivity studies of underwater UV irradiance to changes in atmospheric and oceanic optical properties show that solar-zenith angle, cloud transmittance, water optical properties, and total ozone are the main environmental parameters controlling absolute levels of UVB (280–320nm) and DNA-weighted irradiance underwater. Monthly maps of underwater UV irradiance and DNA-weighted exposure are calculated using monthly-mean SeaWiFS chlorophyll and diffuse attenuation coefficient, daily SeaWiFS cloud fraction data, and the TOMS-derived surface UV irradiance daily maps. The results include global maps of monthly average UVB irradiance and DNA-weighted daily exposures at 3m and 10m, and depths where the UVB irradiance and DNA-weighted dose rate at local noon are equal to 10% of their surface values.

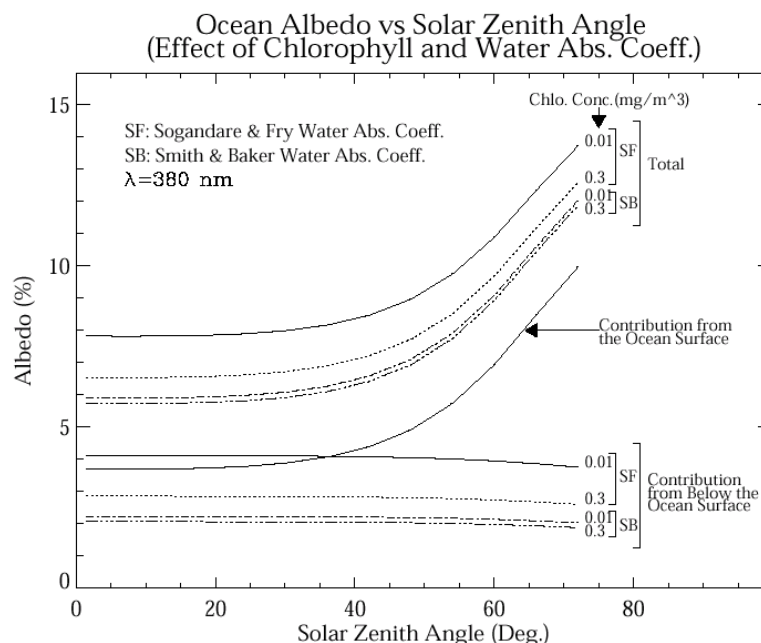


Figure 6-30. Ocean Albedo vs. Zenith Angle and Chlorophyll Concentration at 380 nm. This figure shows that the main contribution to the satellite-retrieved 380 nm radiances from the ocean comes from the surface reflection and from underwater in approximately equal amounts. Retrieval of new ocean properties using UV wavelengths requires knowledge of surface conditions and accurate radiative transfer modeling.

The relationship between chlorophyll concentrations and the 380 nm water-leaving radiances (Figure 6-30) enables us to deduce the amount of chlorophyll from radiance measurements. Of particular interest are recent findings that the ratio of 340 to 380 nm ocean reflectivities are reversed from that of clean water when chlorophyll-bearing phytoplankton is present and mycosporine amino acids, minerals, and other UV-absorbing substances are absent (Figure 6-31). TOMS data indicate that this condition prevails throughout most of the open ocean. The results show that the UV channels can be used to distinguish between types of materials present in the ocean. This finding should lead the way towards future designs for ocean-observing satellite instruments.

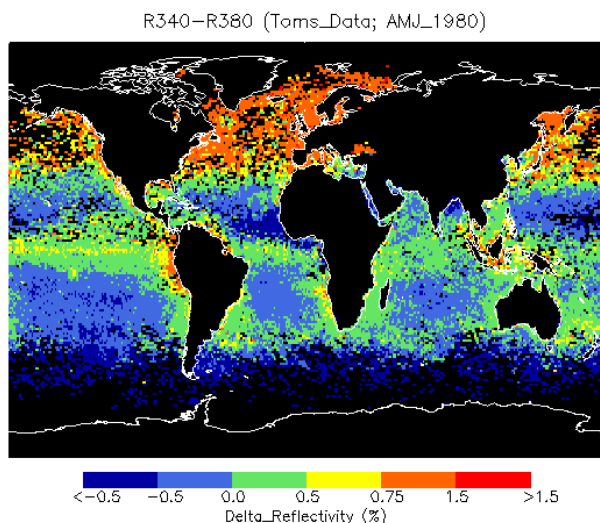


Figure 6-31. TOMS UV reflectivity difference showing chlorophyll patterns that match SeaWiFS data

Jay R. Herman, Code 913 (Jay.R.Herman.1@gsfc.nasa.gov)

Simulating Global Distributions of CO₂

The Earth's climate is changing as a result of human activity, including the emission of greenhouse gas chemicals. Carbon dioxide (CO₂) constitutes the largest current and projected manmade source of climate forcing [*Intergovernmental Panel on Climate Change*, 2001]. Yet, in spite of carbon dioxide's primary importance in climate forcing, large uncertainties exist in the global carbon budget. We must resolve these uncertainties before we can reliably predict the impact of greenhouse gas emissions and devise remedial strategies.

Determining the fate of manmade source gases requires numerical simulation of the transport of CO₂ (and other tracers such as CO, CH₄, and biomass burning tracers). Understanding the exchange of CO₂ between the ocean surface, the terrestrial biosphere, and the atmosphere is critical to understanding the global carbon cycle and what processes determine the atmospheric concentration of CO₂. We conduct transport simulations of CO₂ to better understand how meteorological variability contributes to changes in CO₂ and to better quantify the magnitudes of the surface sources and sinks. A further goal of the simulations is to provide realistic concentration profiles and spatial gradients for determining remote-sensing instrument requirements. The 3-D distributions of atmospheric CO₂ permit instrument developers to estimate sources of error and determine allowable bounds on instrument sensitivity for making meaningful measurements.

The simulation shown in Figure 6-32 was run using monthly average grids of surface fluxes and real-time 3-dimensional wind data from a prototype version (fvDAS) of the assimilation system run by Goddard's DAO. The example day shows the correspondence between the location of the surface sources and sinks and the resulting regions of enhanced and diminished CO₂ in the lower atmosphere (near 850 mbar or about 1500 m MSL). The effects of transport are also seen in the CO₂ distribution. Changes in the average column abundance of CO₂ are produced by the surface forcing as well, but the signal is attenuated relative to that near the surface.

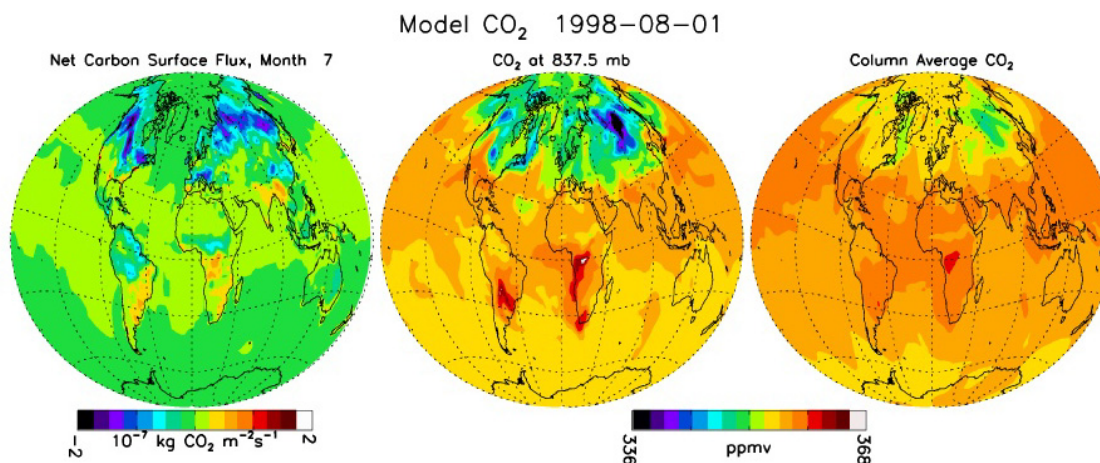


Figure 6-32. Global distribution of input net surface sources and sinks, calculated CO₂ distributions in the lower atmosphere, and column CO₂ for one example day of the simulation. Each color on the CO₂ scale represents 2 ppmv.

With meteorology from data assimilation, such transport runs provide the basic framework to analyze existing (and proposed) measurement data on a point-by-point basis. We compare our simulation with observed CO₂ concentration gradients on a daily, seasonal, regional, and interhemispheric basis to examine the consistency of sources and sinks. Figure 6-33 compares the simulation with surface data at four sites for 1 year. This comparison shows 1) the large seasonal cycle of CO₂ in the Northern Hemisphere driven by exchange with the terrestrial biosphere; 2) the difference in the interhemispheric gradient between the model and data, from which a “missing sink” for CO₂ has been inferred for the Northern Hemisphere; and 3) a significant correlation between the model and data for fluctuations on synoptic (3–5 day) time scales.

Satellite observations of CO₂ with adequate precision and resolution would substantially increase our knowledge of the atmospheric CO₂ distribution and thereby improve our understanding of the global carbon budget. The measurement requirements are challenging, however, since the variation in atmospheric CO₂ is small relative to background levels and most of the variability occurs near the Earth’s surface. Several instrument approaches with a wide range of sampling characteristics are under consideration for measuring CO₂ from space. The spatial and temporal variability of atmospheric CO₂ must be considered in designing potential satellite instruments and in evaluating the potential of proposed methods for inferring fluxes. CO₂ simulations are used as inputs to radiative transfer sensitivity studies needed for algorithm development. In addition, we have begun to investigate the ability of potential satellite instruments with a variety of orbits, horizontal resolutions, and vertical weighting functions to capture the variation in the modeled CO₂ fields. Finally, because our simulations use assimilated meteorology, they will be useful for relating satellite, ground-based, and aircraft observations for satellite calibration/validation and intensive field campaigns.

Future simulation work is aimed at exploiting these methods to better constrain CO₂ sources and sinks, to improve the formulation of transport in the model, and to refine the instrument requirements for remote sensing of atmospheric CO₂. Our long-term goal is assimilation of CO₂ data, including satellite-based CO₂ measurements. This approach is expected to lead to resolution of the global carbon budget and to improved prediction of future climate change and response.

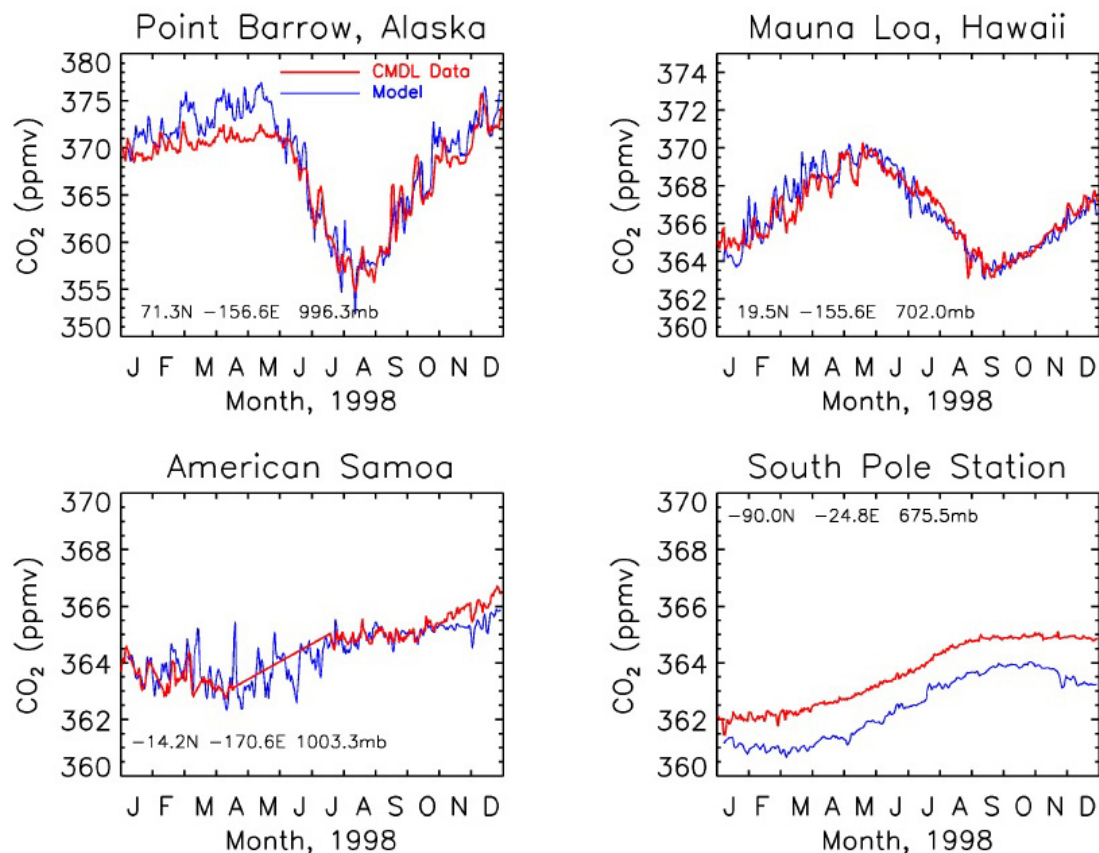


Figure 6-33. Comparison of model output for 1998 with daily measurement data at four sites. CO₂ data is provided by the National Oceanic and Atmospheric Administration, Climate Modeling and Diagnostics Laboratory, Carbon Cycle Group.

Randy Kawa and Arlyn Andrews, Code 916 (Stephan.R.Kawa.1@gsfc.nasa.gov)